2014

Preliminary analysis on the global features of the NCEP CFSv2 seasonal hindcasts

Advances in Meteorology, New York, v. 2014, p. ID695067/1-ID695067/21, 2014
http://www.producao.usp.br/handle/BDPI/46496

Hindawi Publishing Corporation
Advances in Meteorology
Volume 2014, Article ID 695067, 21 pages
http://dx.doi.org/10.1155/2014/695067

Research Article

Preliminary Analysis on the Global Features of the NCEP CFSv2 Seasonal Hindcasts

Gyrlene A. M. Silva, Lívia M. M. Dutra, Rosmeri P. da Rocha, Tércio Ambrizzi, and Érico Leiva

Institute of Astronomy, Geophysics and Atmospheric Sciences, University of São Paulo, São Paulo, 05508-090 SP, Brazil

Correspondence should be addressed to Gyrlene A. M. Silva; gyrlene@gmail.com

Received 26 June 2013; Revised 12 October 2013; Accepted 24 October 2013; Published 19 January 2014

Academic Editor: Klaus Dethloff

The representation of the CFSv2 ocean-atmosphere ensemble hindcasts is investigated during Dec-Jan-Feb (DJF) and Jun-Jul-Aug (JJA) from 1983 to 2010. The skill anomaly correlations showed that in some continents the forecasts do not have dependency with changes in the initial conditions. Also, in both seasons the model has a higher skill at the 0-month lead time with the largest spatial biases occurring over the North America, South America, and Oceania. Over the continents the largest biases in the nonlinearity of El Niño minus La Niña events are found over the eastern South Africa, part of Oceania, and central-southeastern parts of South America. During DJF the main biases are related to double-ITCZ, strengthening of SPCZ, and deepening of the Aleutian and Icelandic low pressures. The simulation of a warmer SST on the eastern of most austral oceans, the strengthening (weakening) of the Subtropical (Polar) Jet over the Southern Hemisphere, and the weakening of the zonal circulation near the Antarctic continent are also found in both seasons. Over the central-eastern Equatorial Pacific a cooler bias in SST is found during JJA. These biases are interpreted by analyses of the simulated global mean-state and their impact on the main patterns of variability.

1. Introduction

It is fair to say that the Ocean-Atmosphere Global Climate Models (OAGCMs) have become indispensable tools for the climate sciences. Despite the complexity of the climate system, many efforts have been made to improve the climate modeling in recent years. The Climate Forecast System version 2 (CFSv2) model is one example of such progress whose hindcasts and real-time operational forecasts have been provided by the National Centers for Environmental Prediction (NCEP) since March 2011. The hindcasts (reforecasts) are designed to test the models; that is, inputs from the past climate are used to the forecasts and allow evaluating how well the predictions approach to the observed climate. CFSv2 is initialized by the CFS Reanalysis (CFSR) that cover the period from 1979 to present and the main characteristics are described by Saha et al. [1].

The hindcasts performance can be assessed by many metrics and some recent papers have focused on assessing the global CFSv2 ability. For the 1982–2009 period Yuan et al. [2] and Wood et al. [3] provided a first look on the CFSv2 hydrological seasonal forecasting skill by comparing it with the CFSv1 reforecasts. Over the continents the CFSv2 increases the skill for monthly surface air temperature and precipitation by 37% and 29%, respectively, compared to CFSv1 [2].

The representation of the intraseasonal variability in CFSv2 is described by Weaver et al. [4]. They discussed that the simulation of this temporal scale continues to be a challenge in CFS versions 1 and 2 due to the strong eastward propagating variance of convection and wind fields. Xie et al. [5] reported that the bias in the CFSv2 land precipitation reforecasts present regional and seasonal variations that appear as a nonlinear function of the target precipitation intensity. Also, the authors demonstrated the preliminary effectiveness results for correction based on probability density function. A comparison of the CFSv2 prediction skill and biases over the Tropical Pacific Ocean for 1982–1998 and 1999–2010 periods is reported by Xue et al. [6] and Barnston and Tippett [7]. According to the authors the higher skill of

this system during 1982–1998 is probably related to the weak observed climate variability in the 1999–2010 period.

The design of the intraseasonal, 9-month reforecasts, and the real-time operational forecasts in terms of skill among CFSv2 and its predecessor is described by Saha et al. [8]. In terms of seasonal prediction, a substantial improvement in the predicted 2-meter air temperature over the global land and in the temperature trends is attributed to the large amount of prescribed greenhouse gases in CFSv2. Nevertheless, the model does not present an increase of the skill in the forecasting of global land precipitation, whereas many improvements occurred in the sea surface temperature (SST) over most of the global oceans, particularly in the extratropics. Over the tropical Pacific Ocean the CFSv2 skill is slightly lower than CFSv1 during boreal winter (JJA) periods. This is related to the subsurface initial states of CFSR that predict warmer mean SST after 1999, perhaps due to the introduction of the Advanced Microwave Sounding Unit (AMSU) satellite data. According to Barnston and Tippett [9] the *a posteriori* treatment of these biases with two separate corrections improves the CFSv2 correlation scores such that they exceed those of CFSv1 at most times of year and at most lead times.

The present study examined the area-average skill over the continents, the interannual variability, the global-mean state, and the main patterns of variability over the Equatorial Pacific and extratropics in both hemispheres produced by the CFSv2 model. The analyses compare the CFSv2 hindcasts with the observations and reanalyses. Emphasis is placed on a preliminary discussion of dynamical reasons for the estimated biases of CFSv2 hindcasts.

The methodology used here differs from previous studies that focus more specifically on some regions of the globe or do not show the global linkage between the simulated ocean-atmospheric circulations. In our analyses the emphasis is on Dec-Jan-Feb (DJF) and Jun-Jul-Aug (JJA) seasons of the 1983–2010 period. The area-average skill and the interannual variability of the hindcasts over the continents for 0–3 month-lead times and the global-mean spatial biases for the 0-month lead are accessed. Also, the nonlinear sign of the interannual variability in total precipitation is investigated by the difference between El Niño (EN) minus La Niña (LN) events based on the departure of the neutral events. Finally, a comparison of the main patterns of variability over the Equatorial Pacific and the extratropics in both hemispheres is done by applying the Empirical Orthogonal Function (EOF). This methodology was motivated by the need to extend the evaluation of the CFSv2 to a global analysis whereas the previous evaluation studies are focused on specific areas or do not focus on a discussion of the ocean-atmosphere interaction around the globe.

Our methodology provides important preliminary information essential for many users that need to properly interpret their seasonal forecasts. It should be emphasized that the present analysis does not focus on a comparison between the features of CFSv2 and its predecessor performance or even with previous models. The paper is organized as follows: in Section 2, the dataset and the retrospective seasonal forecasts of variables and methodology are described; the results are discussed in Section 3; the main findings are summarized in Section 4.

2. Materials and Methods

2.1. Model Description. The main technical information about the CFSv2 is described in http://cfs.ncep.noaa.gov/cfsv2.info/Operational.CFSv2.info.ppt which presents the modifications to improve the seasonal climate forecasts of its previous version (CFSv1). The main advances are in the physical parameterizations, increase of both horizontal and vertical resolutions, initialization techniques, large ensemble size, and carbon dioxide concentration setting evolving realistically over time [8].

The atmospheric component of CFSv2 is the Global Forecast System (GFS) model [10] with consists in a triangular truncation T126 (~0.937°) of horizontal resolution and 64 hybrid sigma-pressure levels in the vertical; finite difference method is used in the solution of the equations. The ocean model is the Geophysical Fluid Dynamics Laboratory Modular Ocean Model v.4 (GFDL MOM4) [11] with 0.25° of horizontal resolution in equatorial region (±10° latitude) and 0.5° in other regions of the globe. The MOM4 uses finite difference methods and hydrostatic approximations. The atmosphere/ocean coupling frequency occurs at 30 minutes which represents a higher frequency than the 24 hours used in CFSv1. The MOM4 is also coupled with a 2-level sea ice model [11] from the GFDL Sea Ice Simulator and with the 4-level Noah land surface model [12].

2.2. Hindcasts, Observed, and Reanalyses Dataset. The present analysis is based on Dec-Jan-Feb (DJF) and Jun-Jul-Aug (JJA) seasons from 1983 to 2010 CFSv2 hindcasts, analyses of observations, and reanalysis dataset. In order to compute the seasonal means for the 0-month lead time, a 24-member ensemble comprises the runs initiated in the six different days of a given month (starting on the first day and each five successive days of the month) and for the four times of each day (00, 06, 12, and 18 UTC). All runs start on the same month of each season. Specifically, mean fields for DJF (JJA) were obtained with CFSv2 hindcasts initialized at 00, 06, 12, and 18 UTC of 1st December (June). For the 1-, 2-, and 3-month lead times all the runs started on the month of Nov, Oct, and Sep (May, Apr, and Mar) for the target DJF (JJA) season, respectively.

For the CFSv2 hindcasts validation, we use the following global monthly mean observational and reanalysis datasets: total precipitation (1° × 1° horizontal resolution) provided by the Climate Prediction Center (CPC) Merged Analysis of Precipitation (CMAP; [13]); 2 m air temperature (0.75° × 0.75° of horizontal resolution) from the European Reanalysis (ERA-Interim; [14]); sea level pressure (SLP), wind-stress, geopotential height at 500 and 850 hPa levels, and zonal wind at 200 hPa level from the reanalyses 2 (2.5° × 2.5° of horizontal resolution) (R2; [15]); Optimum Interpolation v2 OISSTv2 (1°× 1° of horizontal resolution) [16] here referred to as observed SST dataset.

The most adequate procedure to validate the model outputs is being compared with true observation based data. However, the comparison with reanalyses data is also justified since there are no global data covering a long time period available for many variables. Besides, the reanalyses are a reasonable approximation of the real state of the atmosphere. CMAP data set is derived from a combination of rain gauge observations and satellite estimates and it is widely used in many studies based on regional (Silva and Mendes [17]; among others) or global analyses (Dore [18]; Saha et al. [19]; among others). The choice of this precipitation dataset instead of the R2 or ERA-Interim precipitation is to detect the strong global spatial variability inherent in rainfall that requires the use of estimative based on satellite observations mainly over the oceans and the remote regions of the globe. The observed SST dataset used in the present study is also used as input in CFSR [8].

2.3. Methods. For both DJF and JJA seasons we compute the area-average of the hindcasts (considering the lead times 0, 1, 2, and 3 months) for the total precipitation and air temperature at 2 m over each continent. The hindcasts skill is obtained based on the anomaly correlations as a measure of interannual variability. These area-average anomalies hindcasts for precipitation and air temperature at 2 m were compared with the CMAP and ERA-Interim data, respectively. The four lead times were analyzed to examine whether closer initial conditions can improve the forecasts performance. For the 0-month lead time the spatial pattern of the ensemble global-mean of the hindcasts is compared with the CMAP, R2, and SST datasets for each season. This constitutes an important measure of the hindcasts quality.

To facilitate the results visualization, the total precipitation was normalized to the interval $[0, 1]$ by min-max formula similar to Sajikumar and Thandaveswara [20] and Leung [21]:

$$v'(i) = \frac{v(i) - \min_i v(i)}{\max_i v(i) - \min_i v(i)}. \quad (1)$$

A posterior normalization to the interval $[-1, 1]$ was also made assuming that

$$v'' = av' + b. \quad (2)$$

To find a and b we assume that when $v' = 0$, $v'' = -1$ and when $v' = 1$, $v'' = 1$. This results in $-1 = b$ and $1 = a + b$ and from which we have $a = 2$ and $b = -1$. Substituting in (2):

$$v'' = 2v' - 1. \quad (3)$$

Note that now v'' is the normalized total precipitation in the interval $[-1, 1]$.

The main mode that explains most part of the large scale climate variance in the tropics refers to the El Niño-Southern Oscillation (ENSO) [22]. The difference in the sign of the interannual variability (El Niño minus La Niña anomalous total precipitation field), for example, simulated by CFSv2 and CMAP, is analyzed for DJF since the ENSO peak phase occurs in this season. ENSO episodes are selected according to the CPC classification, which considers a threshold of ±0.5°C for the Oceanic Niño Index (ONI) (3-month running mean of ERSST.v3b SST anomalies in the Niño 3.4 region (5°N–5°S, 120°–170°W)), based on centered 30-year base periods updated every 5 years (http://www.cpc.ncep.noaa.gov/products/analysis_monitoring/ensostuff/ensoyears.shtml). Using this criterion, during the 1983–2010 period the El Niño events occurred in the years 1983, 1987-88, 1992, 1995, 1998, 2003, 2005, 2007, and 2010, and La Niña events occurred in 1984-85, 1989, 1996, 1999, 2000, 2001, 2006, 2008, and 2009. Here, the year of the DJF season is assigned as the year of Jan-Feb months. As in da Silva and Ambrizzi [23] we computed the EN and LN anomalies based on departures from normal during neutral ENSO years from 1983 to 2010, that is, the differences between EN minus neutral years and LN minus neutral years. This method is more appropriated to explore the nonlinear sign of ENSO episodes on the precipitation.

Through Empirical Orthogonal Function analysis (EOF, [24]) the maximum amount of variance in the seasonal hindcasts and the observed tropical equatorial Pacific SST anomalies during DJF was examined. The purpose here is to compare the simulated and observed spatial and temporal variability of the ENSO pattern captured over all ocean basins (from 15°N–15°S). Unlike in the tropics, where the main pattern of variability is associated with SST anomalies, over the extratropics the variability signal is mainly due to the natural internal atmospheric response. Regarding the main patterns of extratropical variability, the Northern and Southern Annular Patterns are investigated in CFSv2. For the Northern Annular Mode (NAM) we compared hindcasts and R2 first EOF of sea level pressure (SLP) between 20°N and 90°N during DJF. For the Southern Annular Mode (SAM) the first EOF is based on the geopotential height at 850 hPa over 20°S–90°S for the JJA season. Prior to calculating the EOF patterns the time series in each grid point were scaled by the square root of the cosine of the latitude to compute the area weight and then the annual cycles were removed. The area weighting is required to account for the convergence of the meridians in the high-latitudes areas. As in Hurrell et al. [25] and Yu et al. [26], no statistical significant test was applied in the differences once the purpose is to emphasize the physical aspects of such biases. We assume that no statistical test is perfect even if all test null hypotheses assumptions are done. It means that by assuming any significance level there will always be some probability of rejecting the null hypothesis. For the present analysis not matter reject or not reject null hypothesis because our focus is on understanding of the dynamical features in CFSv2.

3. Results

3.1. Area-Average Skill and the Interannual Variability at Short Lead Times. The anomaly correlations between the area-average ensemble-mean hindcasts over the continents and their corresponding verifications dataset are shown for the target seasons of DJF (Table 1) and JJA (Table 2) for 0- to

3-month lead times. We consider low skill for the correlations equal to or below 0.5 and high skill for correlations values equal to or above 0.6.

Comparing both seasons in average JJA exhibits higher skills independent of the continent, month-lead time, or variable. For DJF (Table 1) the poor skill for both the analysed variables are found over the Asian and Antarctic continents. At 0-month lead time for both total precipitation and air temperature at 2 m the highest skills are found over South America (0.7 and 0.9, resp.) and Oceania (0.6 and 0.6, resp.). Except for 1-month lead time over South America all the other lead times show low skill in precipitation. The air temperature at 2 m presents higher skill at 0-month lead over North America, South America, Africa, and Oceania and for all lead times over South America and Africa only. Over some of the continents the changes in initial conditions do necessarily degrade the forecasts performance of both variables as is the case of South America or of air temperature in Africa, for example.

As in DJF, for JJA, the Antarctic continent exhibits the worst skill (Table 2). For both total precipitation and 2 m air temperature at 0-month lead time the best skills occur in Oceania (0.9 and 0.6, resp.), South America (0.6 and 0.8, resp.), and Asia (0.6 and 0.8, resp.). For precipitation at all month-lead times the largest skills are found in Oceania. Nevertheless, for all month-lead times of surface temperature the skill values equal to or above 0.6 are found over all continents except Oceania and Antarctica. It is more evident in JJA than in DJF that in some continents the use of a larger lead time does not change the forecasting performance mainly after the 1-month lead time.

For all lead times, Figures 1 and 2 for DJF and JJA, respectively, present the time series of the area-average hindcasts anomalies over the continents. For the DJF season CFSv2 is more reliable in reproducing interannual variability of total precipitation anomalies in North America, South America, and Europe (Figures 1(a)–1(c)) although there are some differences in intensity. On the other hand, this feature is poorly simulated over Africa, Asia, Oceania (except of 0-month lead time), and Antarctic (Figures 1(d)–1(g)) due to a lesser amplitude in the CFSv2 anomalies than in the verification dataset. The worst performance occurs in the Antarctic continent with CFSv2 simulating precipitation anomalies with opposite signal compared to the CMAP analysis at all lead times, reflected in the smaller skills (Table 1). CFSv2 fairly simulates according to the reanalysis the positive trends in air temperature at 2 m over all continents and month-lead times (Figures 1(h)–1(n)). The best performance of CFSv2 is found over North America, South America, Africa, and Oceania (Figures 1(h)-1(i), 1(k), and 1(m)), while large errors in amplitude and phase occur in Europe, Asia, and Antarctic (Figures 1(j), 1(l), and 1(n)). For all lead times and years the amplitude and phase of the air temperature hindcasts are best simulated in South America and worse for Europe which presents a large dispersion compared to the other continents.

CFSv2 has a large ability in reproducing the observed interannual variability of precipitation for JJA over North America, Asia, and Oceania (Figures 2(d), 2(j), and 2(l)). As in DJF, for the JJA season, the hindcasts represent positive trends in the air temperature at 2 m in large agreement with the ERA-Interim over all continents. However, the CFSv2 hindcasts show some errors in simulating the amplitude of the 2 m air temperature anomalies, mainly in Europe and Antarctica. Except for Antarctica, for all continents at all lead times the error in phase and amplitude of the CFSv2 anomalies present small and moderate values.

3.2. Simulated Global-Mean Fields and Biases

3.2.1. Total Precipitation. The precipitation pattern is a complex field determined by the global water cycle in association with the behavior of many factors such as moisture distribution over the continents, thermodynamics, and dynamical aspects like the SLP pattern, among others. Figure 3 presents the ensemble mean hindcast and its biases (hindcast minus CMAP analysis) for DJF and JJA. It is noted that CFSv2 captures the main observed (figure not shown) features of DJF rainfall fields, such as Intertropical Convergence Zone (ITCZ), South Pacific Convergence Zone (SPCZ), and South Atlantic Convergence Zone (SACZ), and over the subtropics toward middle latitudes it is noted a minimum between 30°S–60°S (Figure 3(a)). However, Figure 3(a) indicates clearly the presence of a double-ITCZ like pattern over center-eastern Equatorial Pacific and Equatorial Atlantic. A secondary precipitation maximum is simulated over the storms tracks in middle latitudes of the winter hemispheres, which is in accordance with CMAP (figure not shown). In terms of intensity and positioning of the main centers of precipitation, during DJF there is a wet bias in the oceanic ITCZ (around 5°N) over the Equatorial Atlantic and central-western Equatorial Pacific (Figure 3(b)). Wet biases are also found in the SPCZ region, central-eastern tropical Indian Ocean, most extension of the North Atlantic and the Tropical South Atlantic, and subtropics and midlatitudes on the oceans in both hemispheres. The most remarkable DJF dry bias occurs near north Australia and tropical western Pacific around the Oceania, southwestern Indian, and southwestern South Atlantic Ocean (near eastern South America) which is a common error in many global and regional modeling studies ([27, 28] and their references). In continental areas, the rainfall is overestimated over most extension of Central and North America, western Europe, central-eastern Asia, the Andes region, and the eastern of tropical South America, whereas rainfall underestimations occur on most of central-southern Africa, northwestern South America, Indonesia, and northern Australia.

For JJA, the main observed (figure not shown) precipitation action centers are also simulated by CFSv2 (Figure 3(c)), but with some differences in intensity. The larger wet bias occurs over most part of tropical northern oceans (around 15°N) associated with a strengthening of the simulated ITCZ (Figure 3(d)). As in austral summer, CFSv2 simulates wet conditions over the South Hemisphere storm tracks regions and most part of the Indian Ocean. Over the continents, positive biases are found over the northern parts of Asia and Europe, most part of central Asia, and Central-North America. A narrow band of negative bias along the center-western of the Equatorial Pacific Ocean would result as

Table 1: Anomaly correlations between the CFSv2 hindcasts and the corresponding total precipitation from CMAP and temperature at 2 m from ERA-Interim over the continents as a function of target DJF season from 1983 to 2010 period for 0- to 3-month lead times.

Lead times	North America		South America		Europe		Africa		Asia		Oceania		Antarctica	
	Total prec.	Temp 2 m	Total prec.	Temp 2 m	Total prec.	Temp 2 m	Total prec.	Temp 2 m	Total prec.	Temp 2 m	Total prec.	Temp 2 m	Total prec.	Temp 2 m
l0	0,5	**0,7**	**0,7**	**0,9**	**0,6**	0,4	0,3	**0,7**	0,3	0,5	**0,6**	**0,6**	0,2	0,5
l1	0,3	0,5	**0,6**	**0,9**	0,4	0,4	0,1	**0,6**	−0,1	0,3	0,3	0,4	0,1	0,3
l2	0,1	0,5	0,5	**0,9**	0,5	0,1	0,1	**0,7**	−0,1	0,3	0,2	0,5	0,0	0,1
l3	0,3	0,5	0,5	**0,9**	0,3	0,3	−0,1	**0,6**	−0,2	0,4	0,3	0,5	0,1	0,4

The higher correlations are in bold.

Table 2: As in Table 1 but for target JJA season.

Lead times	North America		South America		Europe		Africa		Asia		Oceania		Antarctica	
	Total prec.	Temp 2 m	Total prec.	Temp 2 m	Total prec.	Temp 2 m	Total prec.	Temp 2 m	Total prec.	Temp 2 m	Total prec.	Temp 2 m	Total Prec.	Temp 2 m
l0	0,5	**0,8**	**0,6**	**0,8**	0,3	**0,8**	0,3	**0,8**	**0,6**	**0,8**	**0,9**	**0,6**	−0,2	0,2
l1	0,4	**0,6**	0,3	**0,7**	0,5	**0,8**	0,3	**0,7**	**0,6**	**0,8**	**0,9**	0,5	−0,1	−0,1
l2	0,4	**0,6**	0,3	**0,7**	0,2	**0,7**	0,4	**0,7**	0,3	**0,7**	**0,8**	0,5	0,0	0,2
l3	0,4	**0,6**	0,3	**0,6**	0,3	**0,6**	0,3	**0,7**	0,4	**0,7**	**0,6**	0,4	0,1	0,0

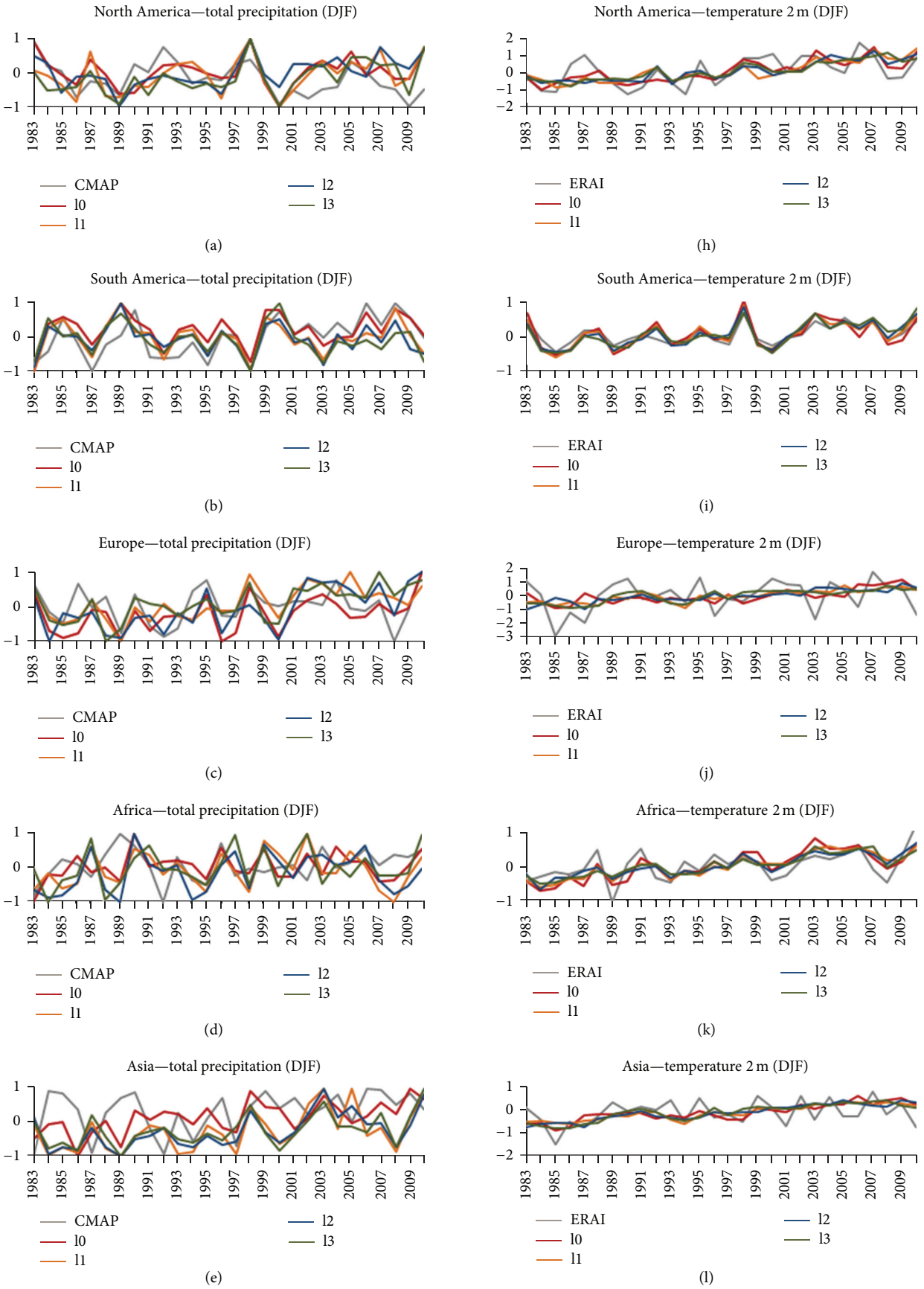

Figure 1: Continued.

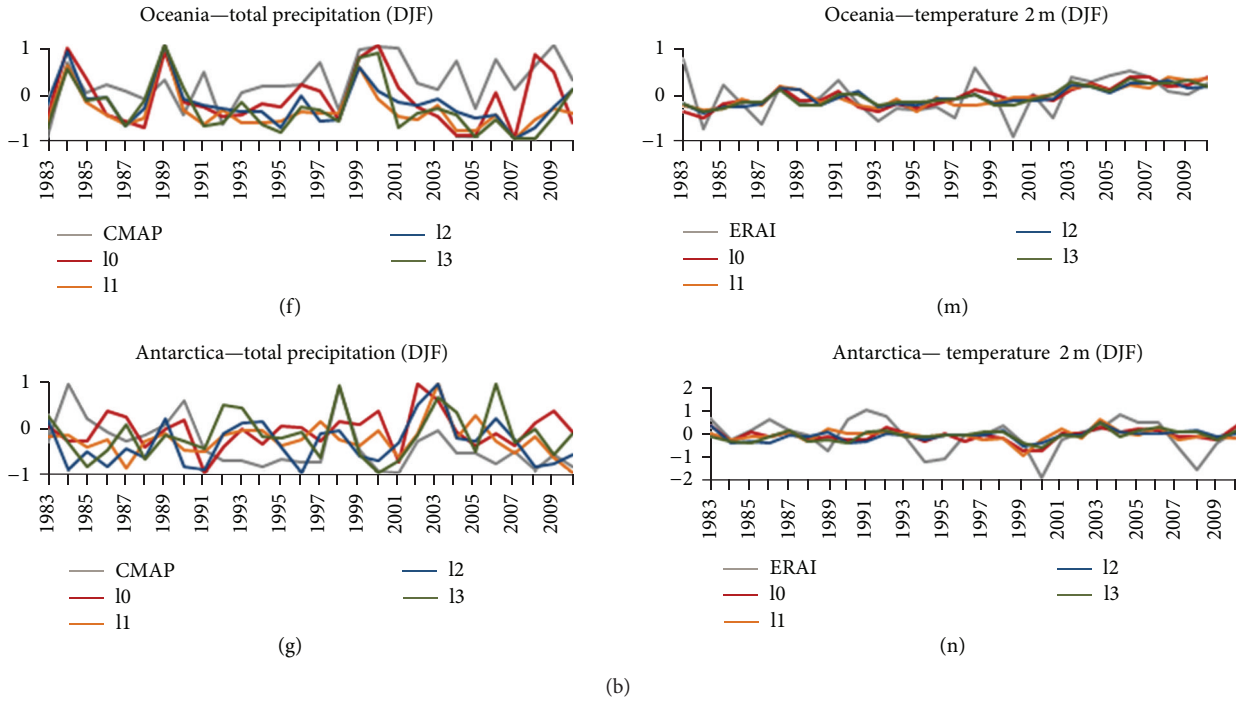

Figure 1: Interannual variability of anomaly hindcasts of CFSv2 at lead 0 (red), 1 (orange), 2 (blue), and 3 (green) for DJF season from 1983 to 2010. The corresponding dataset in gray are on the left column the total precipitation from CMAP; on the right column the temperature at 2 m from ERA-Interim-ERAI.

a compensatory mechanism of the ITCZ strengthening northward. As in DJF, during JJA, the biases over the continent are less widespread than over the oceans. CFSv2 simulates precipitation deficit over the northwestern South America (as in DJF), central Africa, India, eastern Asia (~30°N), and Antarctic. Figures 3(a) and 3(b) indicate that in both seasons the wet (dry) biases are higher over the oceans (continents).

A final comment is that although there are some intensity biases, the latitudinal displacement of ITCZ towards the summer hemisphere is fairly realistic in CFSv2. In both DJF and JJA seasons, the ensemble-mean hindcast simulates a secondary maximum of wet bias between 40°S and 60°S. This indicates a large activity of transient low pressure systems in the Southern Hemisphere storm tracks region.

For the annual mean, Wang et al. [29] mentioned that the double-ITCZ, which is a common deficiency in many coupled models [30], is not apparent in the CFS reanalysis (CFSR) used to initialize CFSv2 hindcasts. Such deficiency occurred in previous coupled ocean-atmosphere models due to the absence of the flux corrections or flux adjustment as suggested by Sausen et al. [31] as a mechanism to remove the climate drift due to the coupling process. According to these authors, the absence of the double-ITCZ-like structure in CFSR would result in improvements on the precipitation in SPCZ, which also leads to a better representation of evaporation minus precipitation. As shown in Figure 3 the simulated double-ITCZ-like structure is still evident in CFSv2 seasonal hindcasts in the eastern Pacific during DJF (Figure 3(a)) and in the tropical Atlantic in JJA (Figure 3(c)). CFSv2 hindcasts do not include flux corrections and more investigations regarding the simulated ITCZ structure in the boreal summer are necessary.

In the following analyses we investigate the large-scales oceanic and atmospheric biases that may be connected with the precipitation biases in Figure 3.

3.2.2. Sea Surface Temperature. SST is a variable used in many climate discussions. The main spatial pattern of the ensemble-mean simulated SST during DJF and JJA (Figures 4(a) and 4(c)) is in large concordance with the observations (figures not shown). For DJF (Figure 4(b)) the large SST errors occur over the Southern Hemisphere related to the warming over the eastern oceans basins (westward of the continents) and around 55°S over all globe. One possible mechanism to explain this warming could be a weakening of the simulated upwelling compared to the observation, which leads to warming SST near the western coast of the continents. The analysis of the wind-stress shown in Section 3.2.4 will be helpful in this interpretation. Over the western oceans basins in the vicinity of eastern continents around the globe CFSv2 simulates normal or colder SST.

In Figure 4(d) the SST biases indicate that in JJA CFSv2 also reproduces warmer conditions in a narrow band in the eastern tropical South Pacific (westward of the South American continent) as in DJF. However, the positive bias is less intense and occupies a smaller area compared to the DJF season. Positive SST biases are also found over the eastern Pacific, from the tropics until high latitudes, and over the North Atlantic, from mid- until high latitudes. The large SST

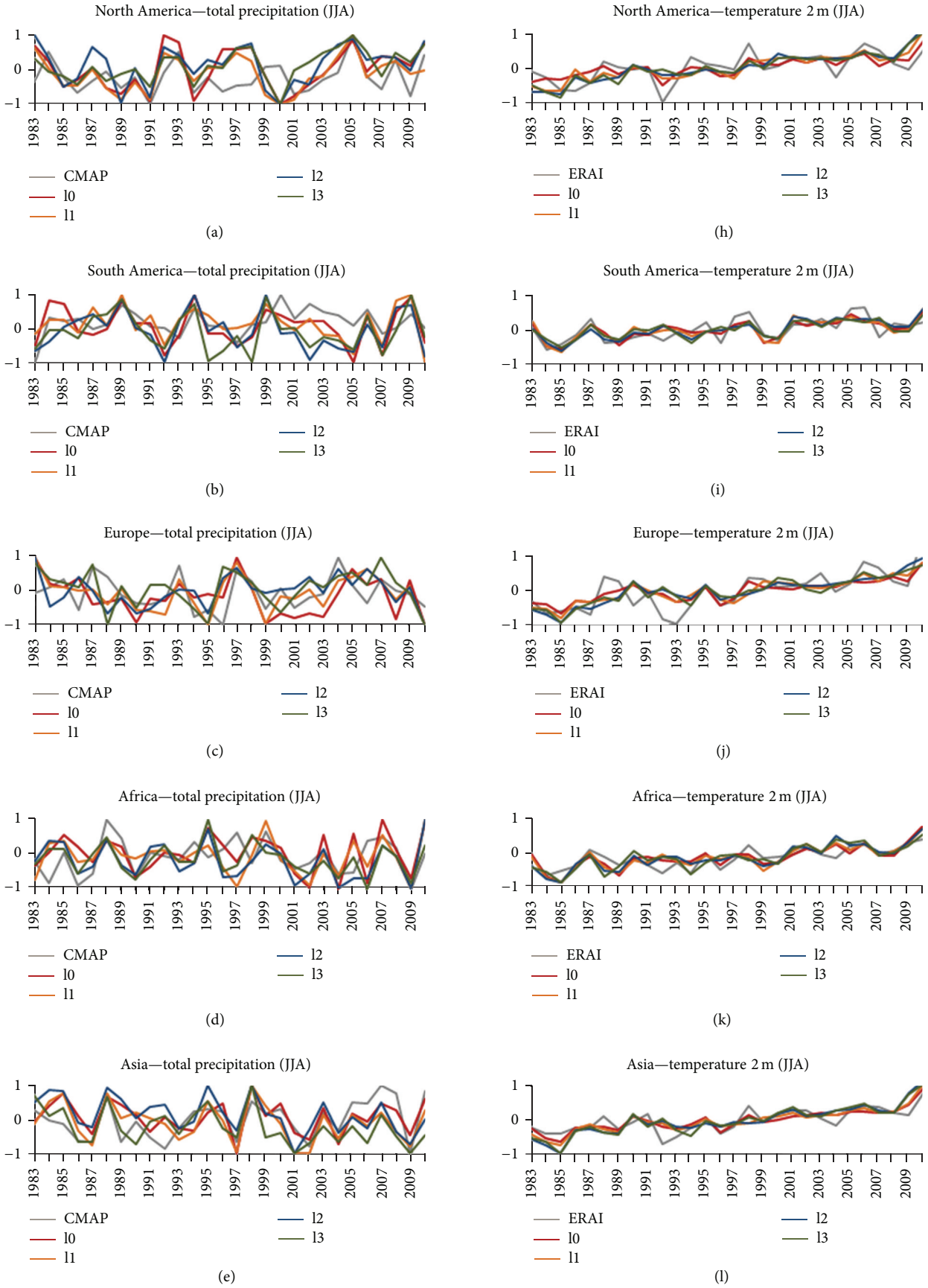

Figure 2: Continued.

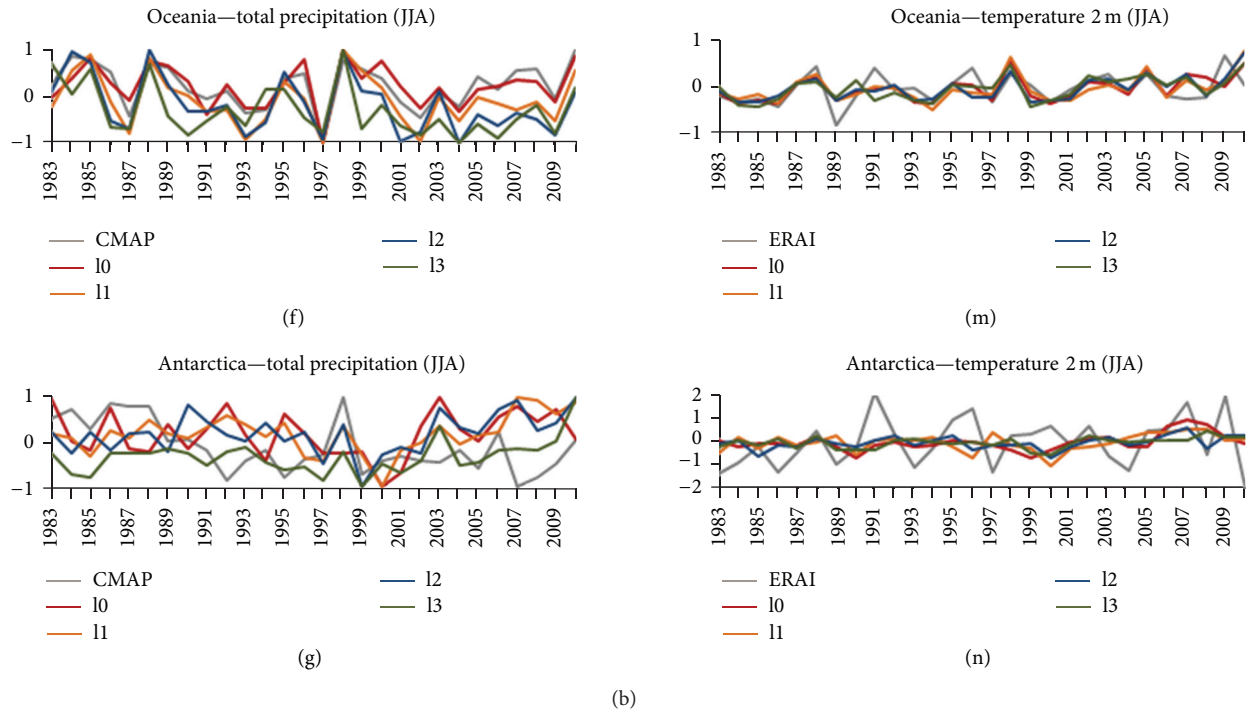

Figure 2: As in Figure 1 but for JJA season.

negative biases are found in the Southern Hemisphere in a latitudinal band in 40–55°S over the equatorial Pacific (180–90°W), while smaller SST biases occur over open oceans in subtropics.

Figure 4(d) is similar to Figure 8 (bottom of the right panel) of [8] showing the annual mean systematic error at 3-month lead time. This indicates that JJA is more important than DJF in reproducing most of the SST annual bias of CFSv2. CFSv2 presents small ability in predicting the mean SST in high latitudes probably due to the limitations in solutions of the ocean-atmospheric or even ice-ocean interactions. An examination related to the possible mechanisms associated with the biases of total precipitation and SST is presented on the next sections.

3.2.3. Sea Level Pressure (SLP). In Figure 5 the ensemble-mean hindcast of the SLP field provides some indication of how the simulation represents the near surface atmospheric circulation, contributing to better understand the simulated precipitation distribution and intensity (Section 3.2.1). Due to the excess of noise the biases in Figures 5(b)–5(d) over high topography are not discussed.

During DJF (Figure 5(a)) the main pressure centers, as the Siberian anticyclone and the Aleutian and Icelandic low pressures, are simulated (Figure 5(a)) in similar positions to the R2 data (figure not shown). Nevertheless, the Aleutian low pressure is more intense and displaced eastward compared to R2. This provides a SLP bias of −4 hPa over midlatitudes of the North Pacific Ocean (Figure 5(b)) in the same region where there is a CFSv2 overestimation of precipitation (Figure 3(b)). Over the Southern Hemisphere, CFSv2 simulates the location of the main SLP centers in reasonable agreement with R2 (figure not shown), with negative pressure biases of ~ −1 hPa covering large part of the oceans. However, negative pressure biases extend through the North Atlantic and Central America associated with the extension of the lower magnitude of the simulated SLP due to the deficiency in the simulation of the Aleutian and Icelandic low pressures. Negative SLP differences of −1 hPa occur in northern latitudes of ITCZ, over the equatorial basins of the Pacific and Atlantic Oceans, showing deeper than R2 convergence zones that would explain the precipitation wet biases over tropical oceans (Figure 3(b)).

In the ensemble-mean hindcast of CFSv2 the semipermanent high pressures over the South Atlantic, South Pacific, and Indian Oceans are weaker than in R2 (Figure 5(b)). This could explain at least in part the SST positive bias over eastern oceanic basins due to the reduction of the upwelling in the western area of continents. An inspection in the simulated wind-stress will help to understand this feature. Around 50°S, the gradient of the biases in the SLP field, with negative (positive) values northward (southward), seems to be associated with more intensity of the baroclinic environment in CFSv2 when compared to R2. Such feature may contribute to the positive bias in the precipitation field (Figure 3(b)) over the midlatitudes and subtropics.

Although the configuration of the simulated oceanic high pressure centers over the Northern Hemisphere during JJA (Figure 5(c)) is in reasonable agreement with R2, a slightly intensification in relation to R2 is noted as shown by the positive bias (Figure 5(d)). The low pressure associated with monsoon flow over Asia is deeper in CFSv2 than in

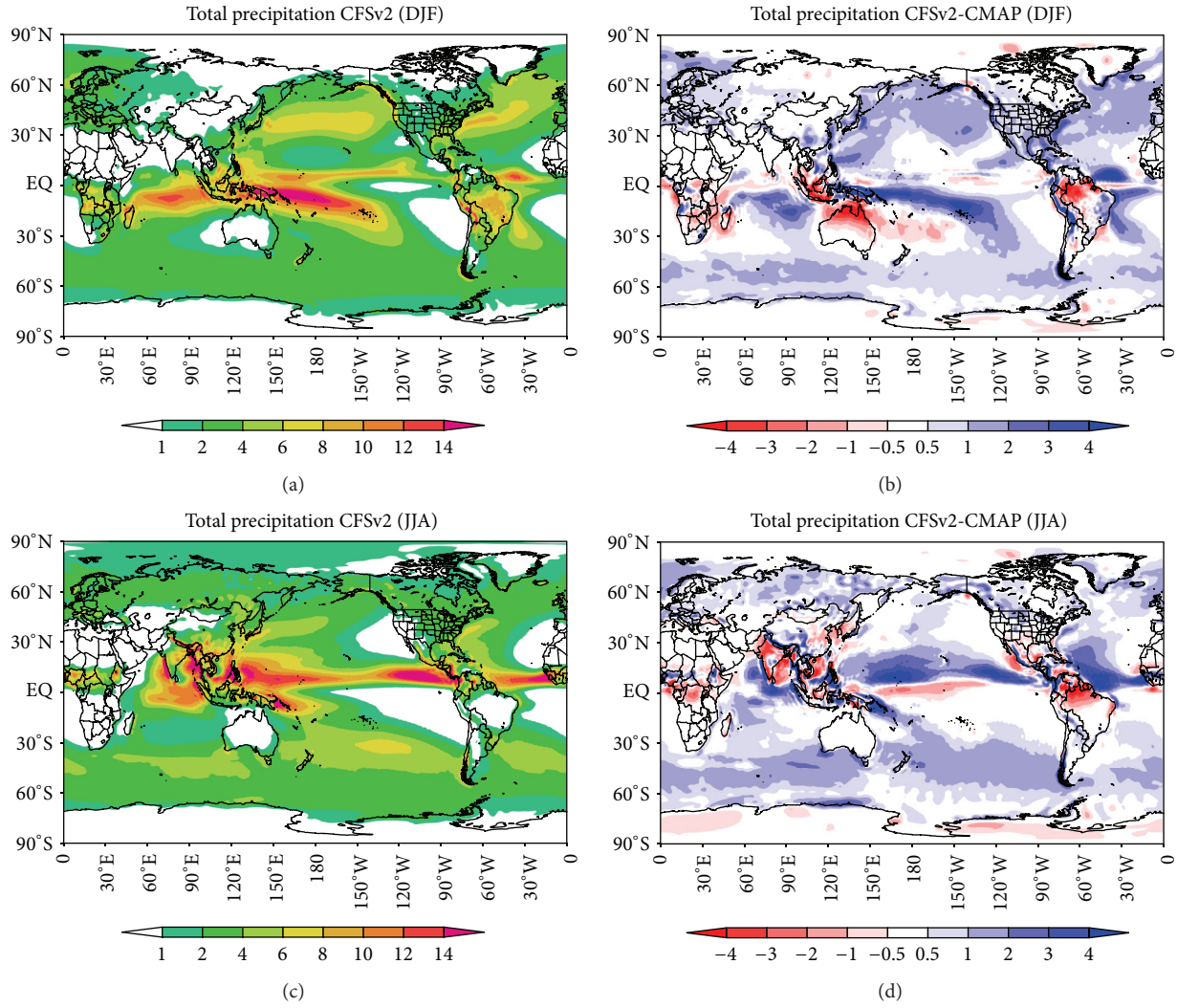

FIGURE 3: Mean total CFSv2 precipitation ((a) and (c)) and differences from CMAP ((b) and (d)) during DJF ((a) and (b)) and JJA ((c) and (d)) at 0-month lead. The climatology period is 1983–2010. Shaded interval is 2 mm/day from 1 mm/day in (a) and (c) and 1 mm/day from 0.5 mm/day in (b) and (d).

R2, implying in the positive precipitation biases over this region (Figure 3(d)). A similar feature related to deeper low pressure might explain the wet bias over the southwestern tropical Pacific Ocean. Positive SLP biases (Figure 3(d)) over the mid-latitudes of the South Atlantic and western Indian Oceans reaching South Africa indicate more intense transient high pressure systems in the CFSv2 hindcasts. As in DJF, in JJA, there are negative SLP biases over the subtropical Pacific Ocean and positive counterpart over the high latitudes southern ocean. This biases pattern may favor the northward shift of the transient activity explaining part of the positive precipitation biases in Figure 3(d).

3.2.4. Surface Wind-Stress. The wind-stress represents the horizontal force of the near surface wind on the sea surface. This variable is a measure of the vertical transfer of horizontal momentum from the atmosphere to the ocean (negative momentum flux) and it is used as a boundary condition in the oceanic model. We investigate the wind-stress instead of the wind vector at low levels to illustrate the sensitivity of the oceanic model component in CFSv2 to the atmospheric forcing.

Over the North Hemisphere, R2 wind-stress for DJF shows strong cyclonic circulations over middle and high latitudes in the North Pacific and North Atlantic Oceans which are related, respectively, to the Aleutian and Icelandic lows (figure not shown). The climatological northeastern wind-stress vectors with 0.15 N/m^2 of magnitude over the Equatorial Atlantic Ocean occur in response to the predominant northeastern surface winds transporting moisture from the sea to the South America (figure not shown). Other important features are the convergence in ITCZ and the southeast flow related to the meridional upwelling near western coasts in the Southern Hemisphere (figure not shown). Strong northeasterly wind-stress predominates over the whole northern part of western-northern Pacific (from

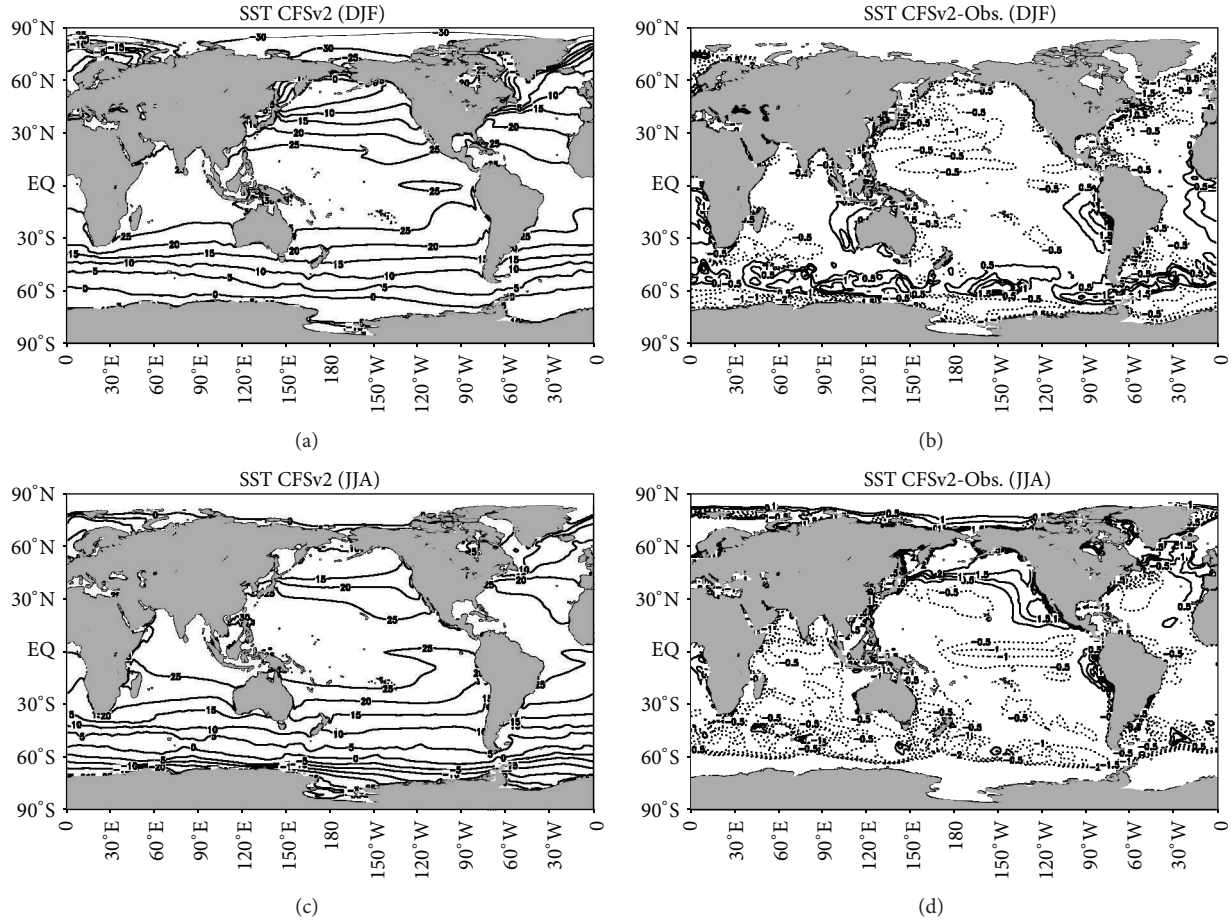

Figure 4: Sea surface temperature (SST) from the CFSv2 ((a) and (c)) and differences from observation ((b) and (d)) during DJF ((a) and (b)) and JJA ((c) and (d)) at 0-month lead. The climatology period is 1983–2010. Contour interval is 5°C in (a) and (c) and 0.5°C in (b) and (d).

the equator to 20°N). For JJA in R2 the mean anticyclonic circulation over the Indian Ocean reflects the persistence of the surface winds associated with the summer Indian monsoon (figure not shown). In this season, over the northern Equatorial Pacific the activity of northeasterly trade winds is displaced to the central basin, while southeasterly trade winds in the western of the basin result from intense monsoon activity.

CFSv2 captures the strong seasonal variation of the wind-stress between DJF and JJA (Figures 6(a) and 6(c)). Moreover, the common features in these seasons are related to the intense westerly wind-stress vectors with a remarkable zonal structure near the Antarctic circumpolar (around 45°S–60°S) in opposition to R2. Also, over the Southern Hemisphere the weak northwesterly bias over the western coast of the continents indicates smaller upwelling over the eastern oceans. This could explain part of the warm bias in SST as shown in Figures 4(b) and 4(d).

During DJF, the most pronounced differences between CFSv2 and R2 are found in middle and high latitudes on the North Pacific and North Atlantic basins (Figure 6(b)). The differences above 0.04 N/m^2 reflect a deficiency in the simulation of the atmospheric forcing driving the magnitude and positioning of the Aleutian and Icelandic low pressures. The bias indicates an anticyclonic gyre due to a deeper Aleutian low in CFSv2 than in R2. This contributes to the cold bias in the simulated SST over the western North Pacific Ocean due to the transport of cold waters from high latitudes. Over the North Atlantic the northeastward flow in middle latitudes and the extension through western tropics indicates that in CFSv2 the Iceland low is less forced by the wind-stress than in R2 dataset. The simulation of the weak Icelandic low could imply in warmer waters in the western North Atlantic in CFSv2 instead of cold waters as shown in Figure 4(b). However, this does not explain the positive and negative biases in the precipitation and SLP, respectively, over the North Atlantic Ocean mid-latitudes. We argue that these biases are related to the persistence of negative SLP and precipitation that leads to colder SST conditions over this area.

Over the Equatorial North Atlantic the southwesterly bias during DFJ (Figure 6(c)) indicates weaker northeasterly trade winds forcing the SST in CFSv2 than in R2. Consequently there is a reduction of the transport of moist air from

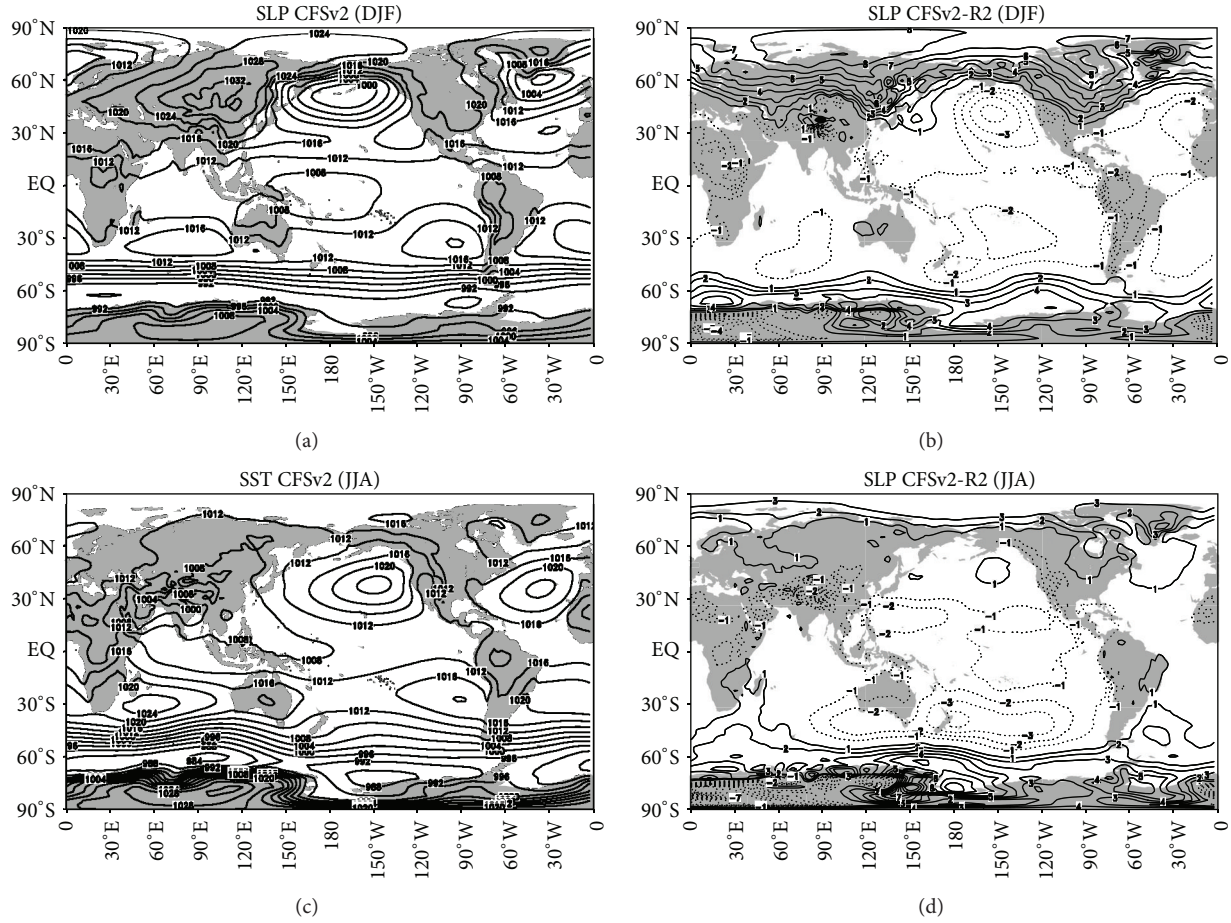

Figure 5: Mean CFSv2 sea level pressure ((a) and (c)) and differences from R2 ((b) and (d)) during DJF ((a) and (b)) and JJA ((c) and (d)) at 0-month lead. The climatology period is 1983–2010. Contours interval is 4 hPa in (a) and (c) and 1 hPa in (b) and (d). Negative contours are dotted.

the ocean towards South America favoring dry conditions over the north of the continent as shown in Figure 3(b). Over the western Pacific, nearest Indonesia, the convergence of southeasterly with northeasterly vectors indicates the strengthening of the wind forcing in the hindcast. Such bias would be associated with the intensification of the convection in SCPZ, inducing consequently colder SST in CFSv2 in this region due to the negative bias over the subtropical Pacific as shown in Figures 3(b), 4(d), and 5(b), respectively. The northeasterly biases over the equatorial Pacific (between 5°N–5°S and 150°E–160°W) also indicate a less zonally orientated wind-stress in CFSv2 than in R2. This may affect the cold tongue regime near the eastern equatorial Pacific inducing the shift of the east-west SST gradient along the equator with implications in the variability of the ENSO pattern in terms of positioning of the SST anomalies. In Section 3.3.1 we examine the ability of CFSv2 in reproducing the spatial and temporal pattern of the ENSO variability to support this interpretation.

During JJA it is noted that wind-stress patterns of CFSv2 are generally similar to R2 over the northern parts of the Pacific and Atlantic basins (Figure 6(c)). However, some biases on the tropics of the North Hemisphere are found in Figure 6(d). Over the tropical North Atlantic the meridional wind-stress is more intense than in R2. This seems to contribute to the ITCZ intensification and its northward displacement, reducing the simulated precipitation over the north-northeast of Brazil (Figure 3(d)). One possible feature to the ITCZ strengthening over the Equatorial Pacific in Figure 3(d) should be the wind-stress bias related to the convergent flow near 15°N in central-eastern of this basin. The persistent ITCZ convection in this region leads to cooler SST favoring part of the negative SLP as shown in Figures 4(d) and 5(d). Over the Arabian Sea and Bay of Bengal the wind-stress is underestimated by CFSv2, resulting in a decaying of the surface warm water transport to the south Asian continent. Dynamically, this favors the reduction of the simulated precipitation amount over South Asia and the Bengal Sea, that is, generating the negative precipitation biases (shown in Figure 3(d)). Such deficiency was also noted in most coupled models [32]. According to our results one possible cause for this error in CFSv2 may be linked to the deficiency in the reproduction of the wind-stress.

Over the western South Pacific Ocean around 20°S in JJA the wind-stress vector biases indicate an underestimation of the atmospheric forcing in the hindcast that do not explain the cold bias in SST. In both DJF and JJA seasons

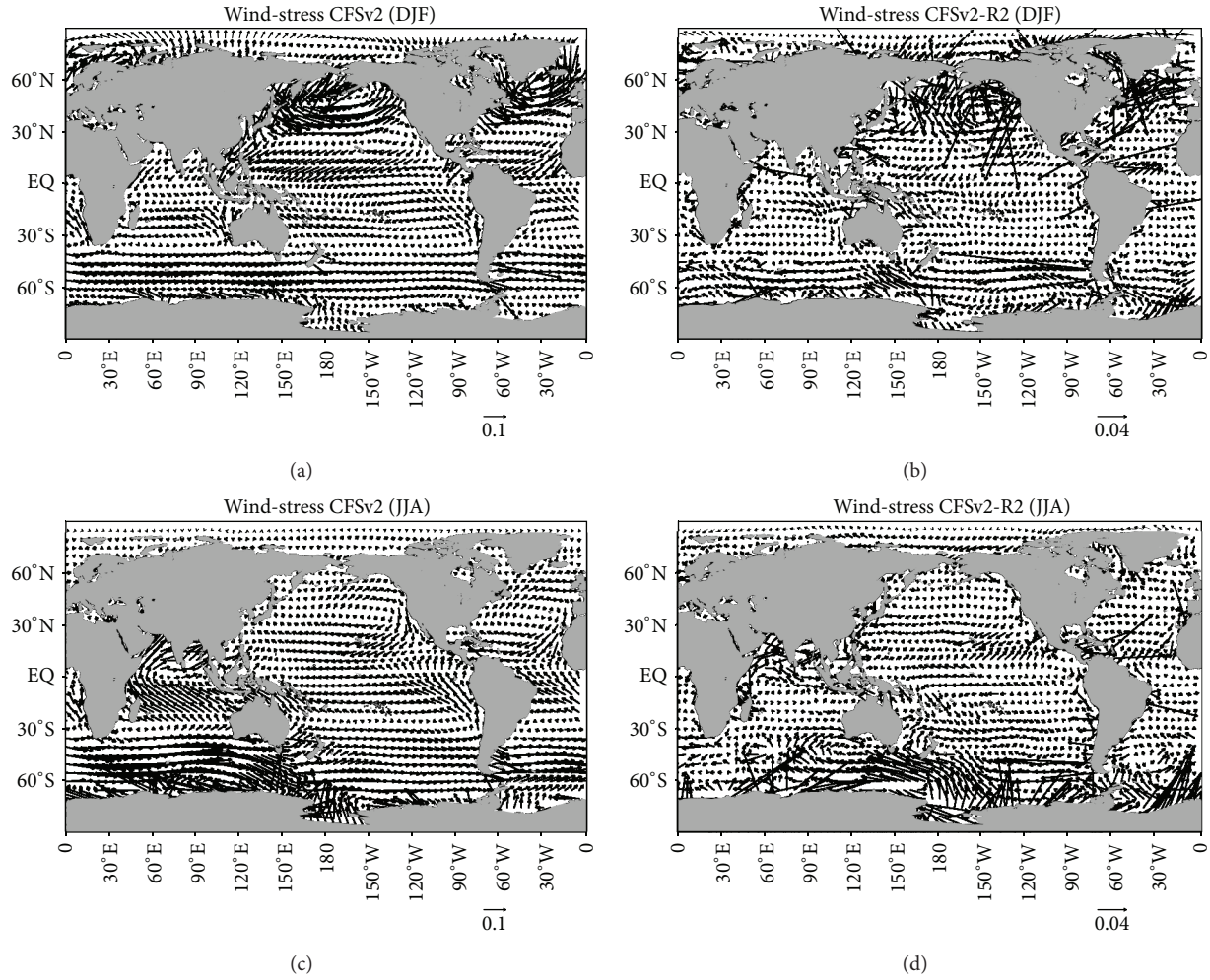

Figure 6: As in Figure 5, but for mean wind-stress vectors. The reference vector corresponds to 0.1 N/m^2 ((a) and (c)) and 0.04 N/m^2 ((b) and (d)).

the simulated wind-stress shows smaller magnitude than R2 in the circumpolar latitudes of the Southern Hemisphere. Dynamically, this indicates that in CFSv2 the atmosphere is transferring less momentum to the surface implying in the weakening of the Polar Jet. The analysis of the geopotential height mean state at 500 hPa and the zonal wind at 200 hPa will be helpful in the interpretation of these biases.

3.2.5. Geopotential Height at 500 hPa. The 500 hPa geopotential height field provides important information about the main action centers of troughs and ridges over the globe and it may be useful in the analysis of the CFSv2 efficiency to simulate the upper atmospheric counterparts of surface cyclones and anticyclones. During DJF, the R2 climatology of the 500 hPa geopotential height indicates that the major troughs are found over Eastern Europe, northeastern Asia, and northern North America, whereas the ridges are located over Russia, western coast of North America, and eastern Atlantic (figure not shown). Figure 7(a) shows that the main simulated patterns of geopotential height at 500 hPa are in agreement with the described R2 climatology, but some differences in the geopotential height values are noted. CFSv2 simulates midlevels troughs and ridges over all globe with smaller values than R2. For DJF the largest negative biases are found over the North Pacific (Figure 7(b)), which is in agreement with the positive bias in precipitation and the deeper low surface pressure shown in Figures 3(b) and 5(b), respectively. This feature reveals the persistence of a tropospheric cold bias mainly over the central-eastern basin that seems to be forced by the atmosphere as seen in the wind-stress bias (Figure 6(b)). Southward of 60°S and in the band 60–25°S CFSv2 presents positive and negative biases, respectively, indicating weak wave pattern in the simulation than R2. Therefore the weak subtropical high pressures in CFSv2 favor the persistency of the low pressures in storm tracks regions, which explain the excessive precipitation in this region (Figure 3(b)).

For JJA, CFSv2 hindcast presents at 500 hPa a large-scale ridge covering the southern part of North America, the subtropical North Atlantic Ocean, and the north part of Africa (Figure 7(a)) which is similar to R2 (figure not shown). In this season, the large biases in the geopotential

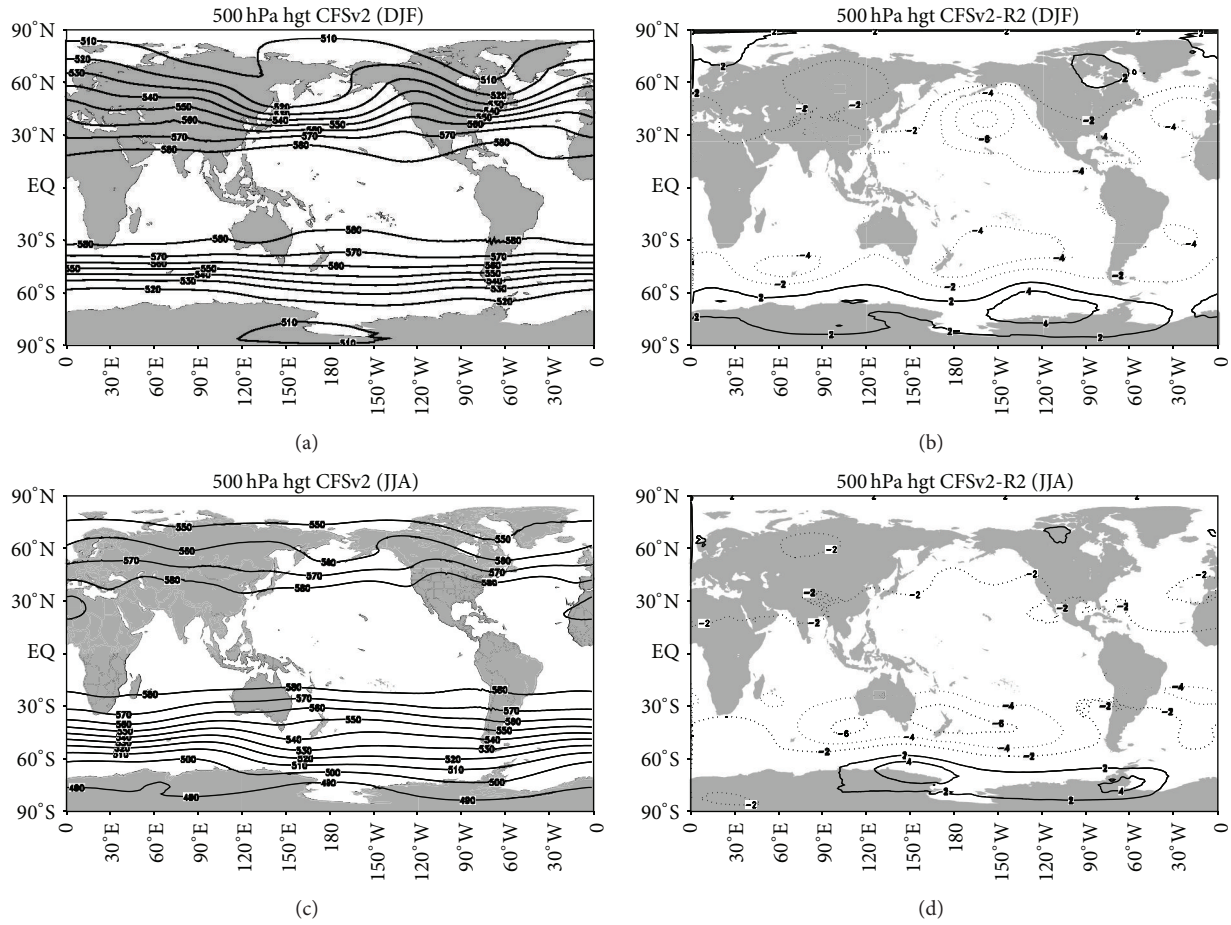

Figure 7: As in Figure 5, but for mean geopotential height at 500 hPa. Contours interval is 10 gpm in (a) and (c) and 2 gpm in (b) and (d). Negative contours are dotted.

height at 500 hPa are found over the Southern Hemisphere (Figure 7(d)). The differences in the winter hemisphere at subtropics and middle-high latitudes suggest a decrease in the wave pattern in CFSv2 as noted in DJF. Also, in both seasons the negative biases over the subtropics contribute to the weakening of subtropical high pressures centers.

3.2.6. Zonal Flow at 200 hPa. The zonal wind at 200 hPa allows an identification of the mean position of the upper-level westerly winds. The westerly jet streams are related to the surface temperature gradients and denote the amplification of the troughs and ridges. The simulated mean zonal wind at 200 hPa for DJF (Figure 8(a)) is fairly similar to the R2 data (figure not shown). Over the Northern Hemisphere, the strongest westerly flows, exceeding 50 m/s, are located in ~30°N in the Western Pacific, Northeast Africa/West Asia, and eastern United States/West Atlantic (Figure 8(a)).

Although the simulated upper-level zonal winds near the equator cover similar areas of R2 the magnitude is smaller, except over the central Pacific (Figure 8(b)). The positive bias seems to be in part associated with the positive precipitation bias, inducing westerly winds over this region. The subtropical and polar jets (STJ and PJ, resp.) on the South Hemisphere are more intense (weak) in CFSv2 than in R2. According to Carvalho et al. [33] this seesaw pattern is mainly associated with the negative South America Monsoon (SAM) phase. Also, the negative (positive) SAM is dominant when warm (cold) SST is observed over the central-eastern Pacific. Therefore, we can argue that CFSv2 has a tendency to simulate more SAM events in the negative phase than the positive phase, which reduces the agreement of the time series of the observed and simulated SAM mode (see Section 3.3.2).

CFSv2 minus R2 upper-level zonal wind (Figure 8(b)) shows a zonally averaged westerly bias in most part of the tropics in association with the positive bias in ITCZ shown in Figure 3(d). Similar to DJF, JJA also shows a strengthening of the STJ and weakening of the PJ in comparison to CFSv2. The higher magnitude of the biases during JJA is more evident during the winter hemisphere which is in concordance with the theory of the zonally symmetric Hadley cell [34] justifying more intense westerly winds during the winter season. These biases are in accordance with positive differences of total precipitation found on the subtropics and mid-latitudes of the Southern Hemisphere. As suggested by Garreaud [35] in his Figure 2, there is a positive correlation between the upper-level zonal flow and the precipitation over midlatitude

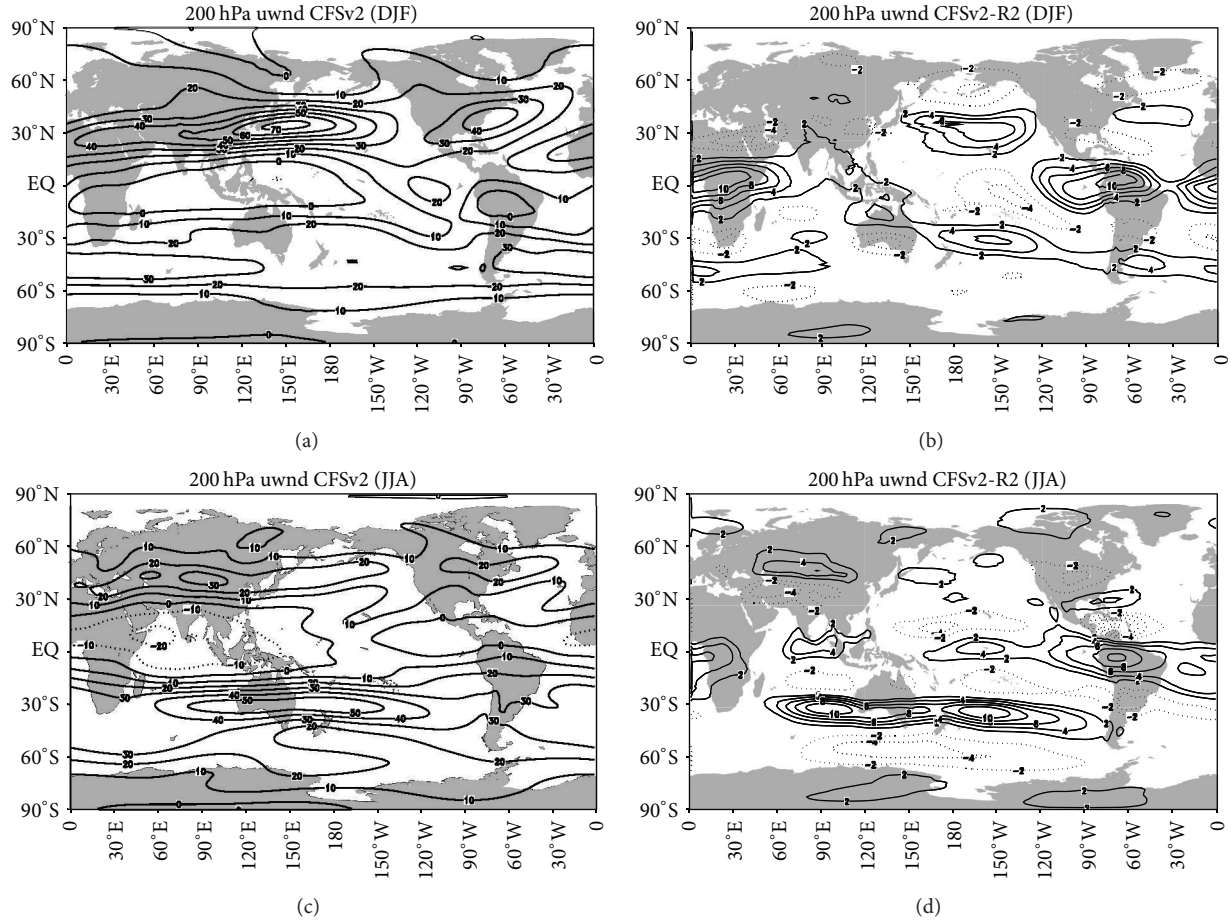

Figure 8: As in Figure 5, but for zonal wind at 200 hPa. Contours interval is 10 m/s in (a) and (c) and 2 m/s in (b) and (d). Negative contours are dotted.

oceans and adjacent continental areas. The stronger westerly upper-level winds contribute to an increase of the cyclones number and/or frontal precipitation due to the growth of baroclinic disturbances.

3.3. Interannual and Extratropical Variability

3.3.1. Interannual Variability. In this section we examined the interannual variability of the CFSv2 hindcasts related to ENSO events. In [7] an important discussion is found related to skill differences in CFSv2 and its predecessor, the CFSv1, in predictions of Nino3.4 SST anomalies for lead times of up to 9 months. The authors focused on discussing the differences related to the CFS model improvements about the 1999 discontinuity in the initial conditions due to CFSR. Our aims in this section differ from those of [7]. We are interested in providing additional information related to the main variability of CFSv2 SST hindcasts over the Equatorial Pacific and its impacts on total precipitation over the globe. For instance, the difference of (EN minus NEU) minus (LN minus NEU) events in total precipitation is analyzed to emphasize the nonlinear relation between the Equatorial Pacific SST anomalies and the respective total precipitation anomalies over the globe. The EOF analysis is applied to SST anomalies over the Equatorial Pacific to provide the main spatial pattern of maximum variance and their temporal behaviour. We emphasize that a comparison between CFSv2 and CFSv1 is not performed in this paper.

Figure 9(a) shows the difference between EN and LN total precipitation anomaly simulated by CFSv2 and the corresponding difference from CMAP (Figure 9(b)). ENSO events were selected based on the CPC classifications described in Section 2.3. From CMAP there is an enhancement of tropical precipitation during EN episodes over and near the central-eastern Pacific, western Indian Ocean, and central-southeast South America that closely follows SST anomalies in the region (figures not shown). Reduced precipitation occurs over South Africa, eastern Indian Ocean, Indonesia, SPCZ, northern Australia, northern South America, and Atlantic ITCZ. In general, as noted in Figure 9(a), CFSv2 is able to capture most of these characteristics. However, some regional biases related to EN minus LN anomalies are found as noted in Figure 9(b) as follows: (1) the negative differences are more (less) intense over the Atlantic ITCZ (northern South America); (2) over the tropical Andes and central and southeast regions of Brazil the negative differences indicate that CFSv2 reproduces opposite pattern of the inter-ENSO anomalies

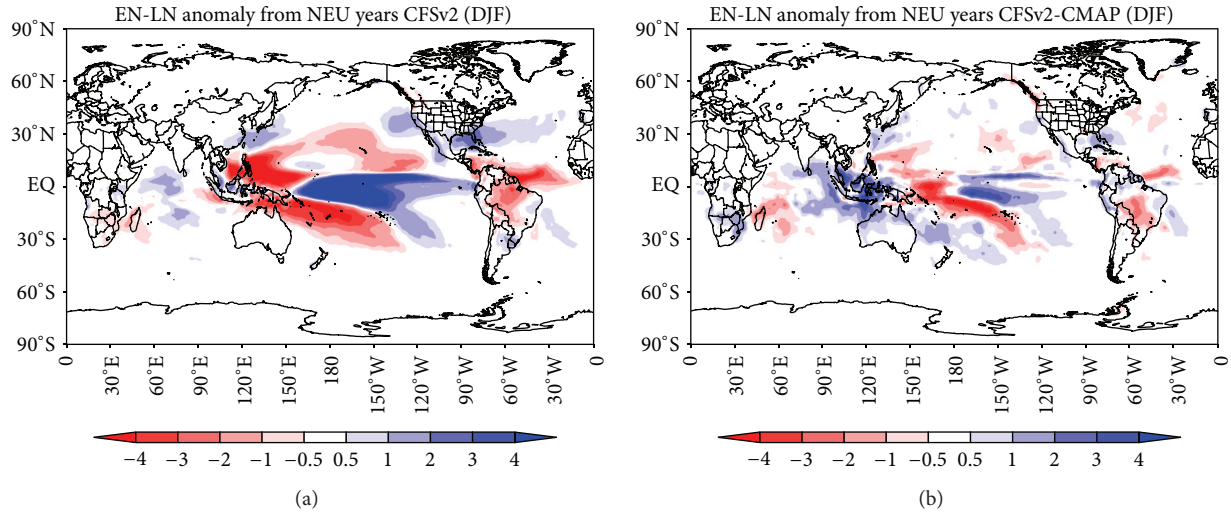

Figure 9: El Niño minus La Niña difference composites of anomalous total precipitation during DJF at 0-month lead time from (a) CFSv2 and (b) difference between CFSv2 minus CMAP. Differences are contoured every 1 mm/day from 0.5 mm/day.

over these regions, which is in contrary to the observations; (3) deficiency in reproducing the EN-LN anomaly over the Indian Ocean (4) the positive bias over the northeast of Brazil (Australia) is associated with positive (neutral) differences in CFSv2 that are not found in CMAP; (5) over the southern North America, Indian Ocean, and Oceania there is a positive bias; (6) there is negative bias over the SPCZ and positive over the ITCZ central Pacific.

An investigation on the CFSv2 capability in representing the spatial and temporal variability of the ENSO pattern is shown in Figure 10. The hindcasts of the ENSO pattern are in accordance with the observed ones (Figures 10(a) and 10(b), resp.), although the maximum positive loadings (≥2.5°C) are displaced to eastern Equatorial Pacific compared to observation. Such shifting in the maximum magnitude of SST anomalies is associated with the bias in the wind-stress mean state (Figure 6(b)). Over 5°N–5°S and 150°E–160°W the less zonally orientation of the wind could influence the positioning of the ascending branch of the Walker Circulation over the western Equatorial Pacific Ocean. The simulated spatial pattern represents 75% of the total variance in the SST fields while in the observation it is 67% which means an overestimation of the captured variance of less than 10%. This could be associated with a tendency of the model to shift the maximum SST anomalies eastward compared to the observations. Figure 10(c) shows the corresponding normalized EOF time series from CFSv2 (black line) and observations (gray line). There is a fairly correspondence between them and the correlation coefficient is 0.97. Also, the strong ENSO events are well reproduced by CFSv2.

3.3.2. Extratropical Variability. The Northern and Southern Annular Modes (NAM and SAM, resp.) are the main extratropical patterns of low frequency variability and their existence is due to internal atmospheric dynamics in middle and high latitudes in both hemispheres. A thorough discussion about the annular patterns can be found in Thompson and Wallace [36]. Figures 11 and 12 indicate that CFSv2 does not have a very good ability in simulating the NAM and SAM spatial structure and that the magnitude of the leading patterns shows some deficiencies possibly due to the bias in the mean state.

The NAM is obtained from the first EOF mode of the SLP field for DJF. In the R2 data (Figure 11(b)) this mode is characterized by centers of action over the North Pacific and North Atlantic Oceans with negative loadings and over polar latitudes with positive loadings. The simulated NAM shows some similarities in terms of location (Figure 11(a)). Nevertheless, on the North Pacific the negative loadings are higher in CFSv2 than in R2 which could be attributed to a bias in the SLP field during the boreal winter in this region due the deeper Aleutian low (Figure 6(b)). The percentage of variance captured by CFSv2 and R2 related to NAM is 31% and 26%, respectively. Based on the Aleutian low bias it could be concluded that the overestimation of the simulated explained variance is associated with differences induced by the natural climate variability between the model and R2. Looking at the EOF time series for CFSv2 (black) and R2 data (gray) a smaller amplitude of SLP anomalies is noted and in some years (e.g., 1991–93) there is an opposite sign resulting in moderate correlation of 0.49 between the series.

The major spatial features related to the shape and orientation of SAM are not well captured by CFSv2 in comparison to R2 (Figures 12(a) and 12(b), resp.). The zonal wavenumber is smaller than in reanalysis. According to Lefebvre et al. [37] the SAM shape is an important factor to be considered because it indicates the direction of the storm tracks flow. Indeed, the simulated SAM accounts for 32% of the captured variance and for R2 it is 26%. It is probably in association with the two larger pair of geopotential height centers captured over the Pacific and the anomalies of opposite sign over the tropical Indian and Atlantic Oceans in comparison with the reanalysis. Such deficiency seems to favor the SLP bias shown in Figure 5(d) and consequently has impact on the

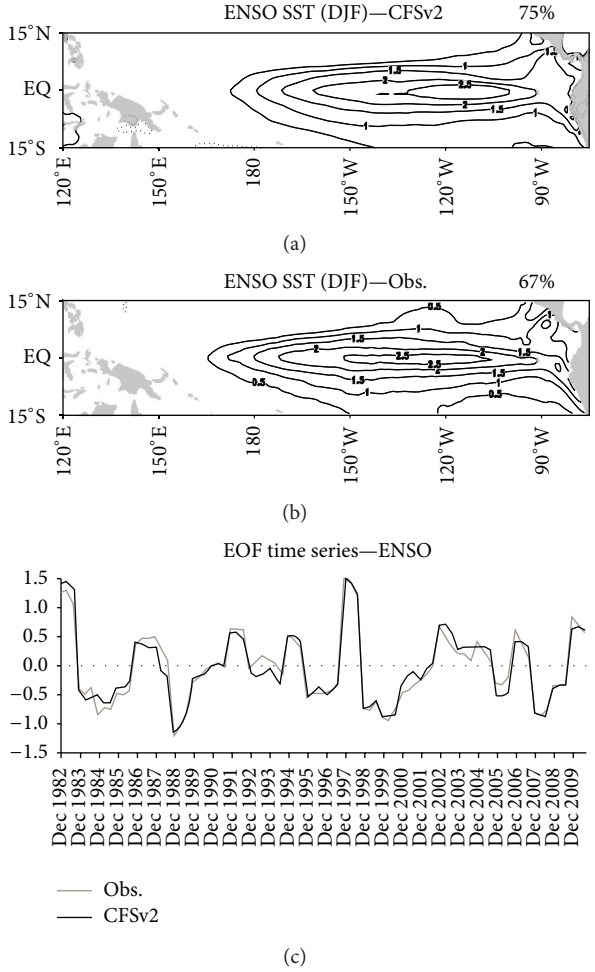

Figure 10: El Niño-Southern Oscillation (ENSO) pattern captured from anomalous SST over 15°N–15°S and 120°–285°E during DJF at 0-month lead for (a) CFSv2; (b) Optimum Interpolation v2 SST (Obs.); (c) the corresponding EOF time series which the gray (black) line is related to Obs. (CFSv2). Contour interval is 0.5°C and negative contours are dotted.

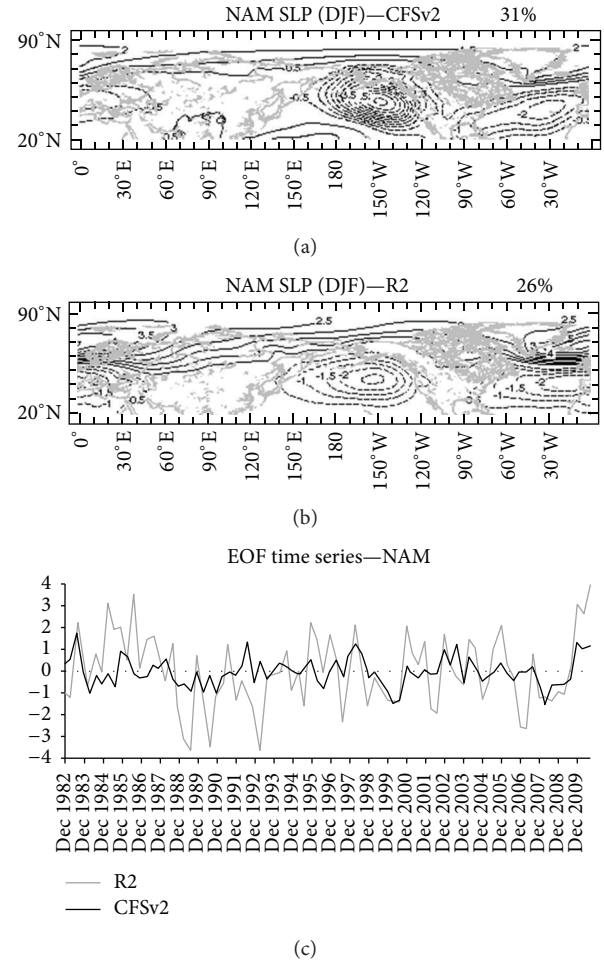

Figure 11: Northern Annular Mode (NAM) captured from SLP anomalies over 20°–90°N during DJF season at 0-month lead for (a) CFSv2; (b) R2 data; (c) the corresponding EOF time series which gray (black) line is related to R2 (CFSv2). Contour interval is 1 hPa from 0.5 hPa and negative contours are dotted. (a) and (b) are adapted from IRI/LDEO Climate Data Library.

bias in precipitation over the dominium. The respective time series of SAM is in Figure 12(c) in which the black (gray) line represents the loadings for CFSv2 (R2). Besides the amplitude of the simulated anomalies that is smaller than reanalysis the model does not reproduce most of the magnitude values implying in a correlation of 0.42 between the time series.

4. Discussions and Conclusions

A preliminary discussion regarding some of the important features of CFSv2 hindcasts over the globe is presented. We analyzed DJF and JJA during 1983–2010. The skill (anomaly correlation) of the ensemble-mean seasonal area-average over the continents and its interannual variability is investigated for four lead times. Further the nonlinear signal of ENSO over the globe, the spatial distribution of the global-mean state seasonal hindcasts, and its main patterns of variability on the tropics and extratropics in both hemispheres are examined.

The air temperature skill during the boreal summer does not present a clear dependency on the lead times used in the seasonal hindcasts, indicating a positive aspect of CFSv2. The hindcasts also have good ability in representing the positive air temperature trends in the interannual scale. Except for South America, the 2 m air temperature amplitude is smaller in CFSv2 than in ERA-Interim.

In both seasons CFSv2 has a higher skill at the 0-month lead time, with the largest biases occurring over North America, South America, and Oceania. Such feature is an important indicative that the skill and bias relationship in CFSv2 should be applied in relative rather than absolute terms. Delsole and Shukla [38] discussed the links between the skill and the bias measures of seven coupled models, which in most regions presented negative skill-bias relationship (except over South America where they found a positive relationship: higher bias and higher skill).

The CFSv2 precipitation at the 0-month lead time exhibits similarities with CMAP even though large biases occur over

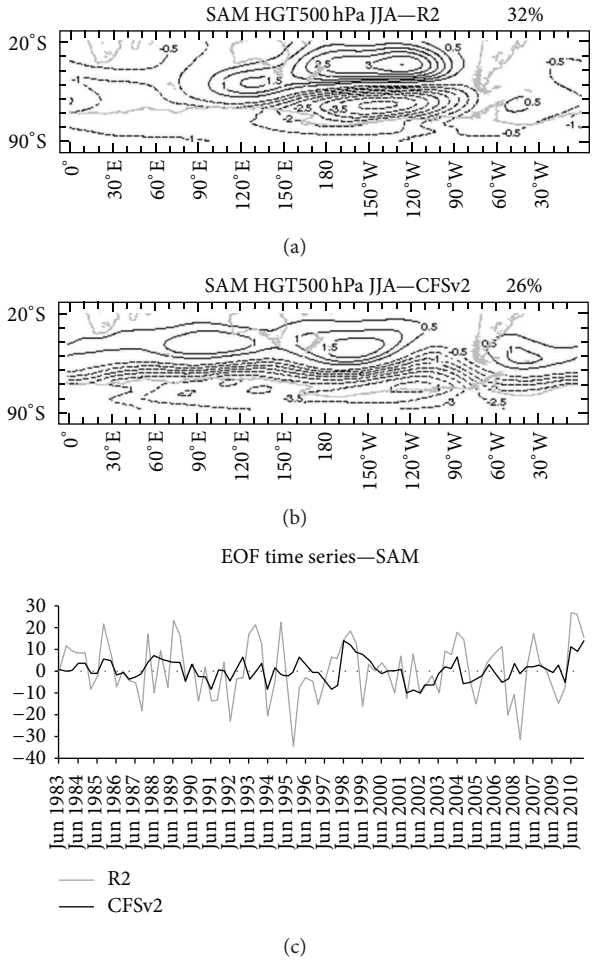

Figure 12: Southern Annular Mode (SAM) captured from mean geopotential height at 850 hPa over 20°–90°S during JJA season at 0-month lead for (a) CFSv2 and (b) R2 data; (c) the corresponding EOF time series which gray (black) line is related to R2 (CFSv2). Contour interval is 1 hPa from 0.5 gpm and negative contours are dotted. (a) and (b) are adapted from IRI/LDEO Climate Data Library.

the oceans. Improvements in CFSv2 were not enough to eliminate the double-ITCZ bias during DJF. This error is mainly associated with the zonally elongated SPCZ that is a common and persistent error of coupled models as reported in previous studies. In response to this error there is a strengthening of SPCZ and dry biases over part of the Equatorial Atlantic. Our results revealed that over the western Pacific (near Indonesia) the convergence of southeasterly and northeasterly wind-stress biases intensifies the convection in SPCZ and its zonal alignment favors cooler SST conditions in the western Pacific.

Part of the warm SST bias over eastern oceans during DJF and JJA could be a result of a slightly upwelling reduction due to the wind-stress bias. For JJA the SST cold bias over the central-equatorial Pacific may be related to a strengthening of ITCZ over the Equatorial Pacific in association with the wind-stress bias near 15°N in the central-eastern basin. More intense and persisting convection in ITCZ in this region inhibits the local solar warming leading to colder SST and also explains part of the negative SLP bias in these regions.

During DJF CFSv2 presents a cold bias in the troposphere, mainly over the central-eastern North Pacific, which would be forced by the atmosphere due to the wind-stress bias. The anticyclonic gyre in the wind-stress bias indicates a deeper Aleutian low in CFSv2 than in R2, contributing to wet biases over this basin. The bias in wind-stress is also connected with a colder CFSv2 SST in the western North Pacific Ocean due to the transport of cold waters from high latitudes.

Another remarkable feature in CFSv2 is the strengthening of the subtropical jet that leads to precipitation overestimations by the persistence of low pressures over subtropical and mid-latitude regions. The circumpolar zonal circulation around the Antarctic is weaker in CFSv2 than in R2 compromising the natural variability representation over the extratropics on the Southern Hemisphere.

Regarding the nonlinearity of EN minus LN events, CFSv2 shows large precipitation biases over the eastern South Africa and Oceania. The simulated ENSO pattern is in reasonable agreement with the observations, a result in agreement with Kim et al. [39] and Barnston and Tippett [7]. The wind-stress bias in the tropics may be associated with the shifting of the maximum loading values compromising the ascending branch of the Walker Circulation in the western Equatorial Pacific.

Considering the reasonable ability of CFSv2 in representing the ENSO interannual variability it is possible to suggest the use of the first EOF time series as explanatory variables in the transfer function downscaling approach. Schubert and Henderson-Sellers [40] discussed that if the structure of the main patterns of spatial variability is orthogonal their associated time series are uncorrelated with each other. An example of recent application using EOF time series as explanatory variable is presented in Silva and Mendes [17].

Regarding the CFSv2 extratropical variability, the errors in the simulated Aleutian low seem to degrade the simulated NAM, with CFSv2 simulating larger percentage of the explained variance (31%) than R2 (26%). The EOF time series of NAM presents moderate correlation with R2 due to the deficiency in the representation of Aleutian low pressure.

The wave pattern associated with SAM is not well reproduced by CFSv2. The model simulates two large geopotential height centers over the Pacific and the anomalies have opposite sign compared with R2 over the tropical Indian and Atlantic. Such deficiency partly explains the biases in the upper-level zonal wind over the tropics and mid-latitudes of the Southern Hemisphere. By comparing the mean-state atmospheric bias presented here a barotropic structure associated with the strengthening (weakening) of the subtropical (polar) jets in CFSv2 is noted.

The major spatial features related to the shape and orientation of SAM are not properly captured by CFSv2 in comparison to R2. The zonal wavenumber in CFSv2 is smaller than in R2. According to Lefebvre et al. [27] the SAM shape is an important factor to be considered because it indicates the direction of the storm tracks flow. The simulated SAM accounts for 32% of the captured variance, while in R2 it is 26%. Such deficiency seems to favor SLP bias with impacts on

the precipitation biases over the dominium. The time series of SAM in CFSv2 have smaller amplitude than R2 and the model does not reproduce most of the magnitude values implying in a correlation of 0.42 between the time series.

Overall evaluations show that although there are large improvements in CFSv2 further investigations are still needed. The model skill and biases identified here are essential for further investigations related to impacts on the prediction skill pattern. Thus, detailed investigations should be carried out to help in understanding in further details the reasons for the CFSv2 deficiencies shown here. A special emphasis on surface fluxes is also important. Furthermore the applications of statistical techniques are required as complementary tool for ensemble improvements as in [17].

Conflict of Interests

The authors declare that there is no conflict of interests regarding the publication of this paper.

Acknowledgments

The authors thank the editor and the three anonymous reviewers whose constructive comments help us improve the paper. Also, they thank NCEP for providing the observational, reanalyses, and modeling data and the ECMWF for their reanalysis. Gyrlene A. M. Silva would like to thank Michael Bell from the International Research Institute for Climate and Society (IRI) for the help in computing the EOF analysis and the Group of Climate Studies from University of São Paulo (GrEC/USP) for providing the physical locations for the model dataset preparation. The authors also thank the INterdisciplinary CLimate INvestigation cEnter (INCLINE/USP) for the support received. Tércio Ambrizzi also acknowledges São Paulo Research Foundation (FAPESP) (Proc. No. 08/58101-9) and National Council for Scientific and Technological Development (CNPq) for partial support.

References

[1] S. Saha, S. Moorthi, H.-L. Pan et al., "The NCEP climate forecast system reanalysis," *Bulletin of the American Meteorological Society*, vol. 91, pp. 1015–1057, 2010.

[2] X. Yuan, E. F. Wood, L. Luo, and M. Pan, "A first look at Climate Forecast System version 2 (CFSv2) for hydrological seasonal prediction," *Geophysical Research Letters*, vol. 38, no. 13, Article ID L13402, 2011.

[3] E. F. Wood, Y. Yuan, and J. K. Roundy, "Enhancing hydrological seasonal forecast by downscaling CFSv2," in *Proceedings of the 36th NOAA Annual Climate Diagnostics and Prediction Workshop*, Science and Technology Infusion Climate Bulletin NOAA's National Weather Service, Fort Worth, Tex, USA, 2011.

[4] S. J. Weaver, W. Wang, M. Chen, and A. Kumar, "Representation of MJO variability in the NCEP climate forecast system," *Journal of Climate*, vol. 24, no. 17, pp. 4676–4694, 2011.

[5] P. Xie, S.-H. Yoo, W. Wang, and A. Kumar, "Correcting the bias in the CFS version 2 land precipitation forecast," in *Proceedings of the of the CFSv2 Evaluation Workshop*, 2012.

[6] Y. Xue, M. Chen, A. Kumar, Z. - Hu, and W. Wang, "Prediction skill and predictability of tropical pacific sea surface temperature in the NCEP CFSv2 retrospective forecast," in *Proceedings of the of the CFSv2 Evaluation Workshop*, 2012.

[7] A. G. Barnston and M. K. Tippett, "Predictions of Nino3. 4 SST in CFSv1 and CFSv2: a diagnostic comparison," *Climate Dynamics*, pp. 1–19, 2013.

[8] S. Saha, S. Moorthi, and S. Wu, "The NCEP climate forecast system version 2," *Journal of Climate*, 2013.

[9] A. G. Barnston and M. K. Tippett, "A diagnostic comparison of CFSv1 and CFSv2 predictions of Nino3.4 SST," in *Proceedings of the CFSv2 Evaluation Workshop*, 2012.

[10] S. Moorthi, H. L. Pan, and P. Caplan, "Changes to the 2001 NCEP operational MRF/AVN global analysis/forecast system," *NWS Technical Procedures Bulletin*, vol. 484, article 14, 2001.

[11] S. M. Griffies, M. J. Harrison, R. C. Pacanowski, and A. Rosati, "A technical guide to MOM4," Tech. Rep. 5:371, GFDL Ocean Group, 2010.

[12] M. B. Ek, K. E. Mitchell, Y. Lin et al., "Implementation of Noah land surface model advances in the National Centers for Environmental Prediction operational mesoscale Eta model," *Journal of Geophysical Research D*, vol. 108, no. 22, pp. 1–16, 2003.

[13] P. Xie and P. A. Arkin, "Global Precipitation: a 17-year monthly analysis based on gauge observations, satellite estimates, and numerical model outputs," *Bulletin of the American Meteorological Society*, vol. 78, no. 11, pp. 2539–2558, 1997.

[14] D. P. Dee, "The ERA-Interim reanalysis: configuration and performance of the data assimilation system," *Quarterly Journal of the Royal Meteorological Society*, vol. 137, pp. 553–597, 2011.

[15] M. Kanamitsu, W. Ebisuzaki, J. Woollen et al., "NCEP-DOE AMIP-II reanalysis (R-2)," *Bulletin of the American Meteorological Society*, vol. 83, no. 11, pp. 1631–1559, 2002.

[16] R. W. Reynolds, N. A. Rayner, T. M. Smith, D. C. Stokes, and W. Wang, "An improved in situ and satellite SST analysis for climate," *Journal of Climate*, vol. 15, no. 13, pp. 1609–1625, 2002.

[17] G. A. M. Silva and D. Mendes, "Comparison results for the CFSv2 hindcasts and statistical downscaling over the northeast of Brazil," *Advances in Geosciences*, vol. 35, no. 35, pp. 79–88, 2013.

[18] M. H. I. Dore, "Climate change and changes in global precipitation patterns: what do we know?" *Environment International*, vol. 31, no. 8, pp. 1167–1181, 2005.

[19] S. Saha, H. van den Dool, and J. Åke, "CFSv2 retrospective forecast and calibration climatologies," 2011, http://cfs.ncep.noaa.gov/cfsv2.info/CFSv2_paper.pdf .

[20] N. Sajikumar and B. S. Thandaveswara, "A non-linear rainfall-runoff model using an artificial neural network," *Journal of Hydrology*, vol. 216, no. 1-2, pp. 32–55, 1999.

[21] K. M. Leung, *Preparing the Data*, Polytechnic University. Department of Computer Science, Finance and Risk Engineering, 2007.

[22] C. Wang and J. Picaut, "Understanding ENSO physics—a review," in *Earth's Climate: The Ocean-AtmoSphere Interaction*, vol. 147 of *Geophysical Monograph Series*, pp. 21–48, AGU, Washington, DC, USA, 2004.

[23] G. A. M. da Silva and T. Ambrizzi, "Summertime moisture transport over Southeastern South America and extratropical cyclones behavior during inter-El Niño events," *Theoretical and Applied Climatology*, vol. 101, no. 3, pp. 303–310, 2010.

[24] D. S. Wilks, *Statistical Methods in the Atmospheric Sciences: An Introduction*, Academic Press, San Diego, Calif, USA, 1995.

[25] J. W. Hurrell, J. J. Hack, A. S. Phillips, J. Caron, and J. Yin, "The dynamical simulation of the Community Atmosphere Model version 3 (CAM3)," *Journal of Climate*, vol. 19, no. 11, pp. 2162–2183, 2006.

[26] W. Yu, Z. Li, and Y. Yuan, "Improvement of the SLP simulation in the coupled AGCM-ocean surface wave model," *Chinese Science Bulletin*, vol. 50, no. 20, pp. 2397–2400, 2005.

[27] S. A. Solman, E. Sanchez, P. Samuelsson et al., "Evaluation of an ensemble of regional climate model simulations over South America driven by the ERA-Interim reanalysis: model performance and uncertainties," *Climate Dynamics*, 2013.

[28] M. S. Custódio, R. P. da Rocha, and P. L. Vidale, "Analysis of precipitation climatology simulated by high resolution coupled global models over the South America," *Suisui Hydrological Research Letters*, vol. 6, pp. 92–97, 2012.

[29] W. Wang, P. Xie, S. H. Yoo, Y. Xue, A. Kumar, and X. Wu, "An assessment of the surface climate in the NCEP Climate Forecast System Reanalysis," *Climate Dynamics*, 2010.

[30] A. Dai, "Precipitation characteristics in eighteen coupled climate models," *Journal of Climate*, vol. 19, no. 18, pp. 4605–4630, 2006.

[31] R. Sausen, K. Barthel, and K. Hasselmann, "Coupled ocean-atmosphere models with flux correction," *Climate Dynamics*, vol. 2, no. 3, pp. 145–163, 1988.

[32] M. Rajeevan and R. S. Nanjundiah, "Coupled model simulations of twentieth century climate of the Indian summer monsoon," in *Current Trend in Science, Platinum Jubilee Special*, pp. 537–568, 2009.

[33] L. M. V. Carvalho, C. Jones, and T. Ambrizzi, "Opposite phases of the Antarctic oscillation and relationships with intraseasonal to interannual activity in the tropics during the austral summer," *Journal of Climate*, vol. 18, no. 5, pp. 702–718, 2005.

[34] I. M. Held and A. Y. Hou, "Nonlinear axially symmetric circulations in a nearly inviscid atmosphere," *Journal of the Atmospheric Sciences*, vol. 37, no. 3, pp. 515–533, 1980.

[35] R. D. Garreaud, "Precipitation and circulation covariability in the extratropics," *Journal of Climate*, vol. 20, no. 18, pp. 4789–4797, 2007.

[36] D. W. J. Thompson and J. M. Wallace, "Annular modes in the extratropical circulation—part I: month-to-month variability," *Journal of Climate*, vol. 13, no. 5, pp. 1000–1016, 2000.

[37] W. Lefebvre, H. Goosse, R. Timmermann, and T. Fichefet, "Influence of the Southern Annular Mode on the sea ice—ocean system," *Journal of Geophysical Research C*, vol. 109, no. 9, Article ID C09005, 2004.

[38] T. Delsole and J. Shukla, "Model fidelity versus skill in seasonal forecasting," *Journal of Climate*, vol. 23, no. 18, pp. 4794–4806, 2010.

[39] H.-M. Kim, P. J. Webster, and J. A. Curry, "Seasonal prediction skill of ECMWF System 4 and NCEP CFSv2 retrospective forecast for the Northern Hemisphere Winter," *Climate Dynamics*, pp. 1–17, 2012.

[40] S. Schubert and A. Henderson-Sellers, "A statistical model to downscale local daily temperature extremes from synoptic-scale atmospheric circulation patterns in the Australian region," *Climate Dynamics*, vol. 13, no. 3, pp. 223–234, 1997.